# Spectroscopic Imaging of Photopotentials and Photoinduced Potential Fluctuations in a Bulk Heterojunction Solar Cell Film

**Justin L. Luria,[†] Nikolas Hoepker,[‡] Robert Bruce,[†] Andrew R. Jacobs,[§] Chris Groves,[⊥] and John A. Marohn[†,*]**

[†]Department of Chemistry and Chemical Biology, [‡]Department of Physics, and [§]Department of Materials Science and Engineering, Cornell University, Ithaca, New York 14853, United States and [⊥]School of Engineering and Computing Sciences, Durham University, Durham DH1 3LE, United Kingdom

**ABSTRACT** We present spatially resolved photovoltage spectra of a bulk heterojunction solar cell film composed of phase-separated poly(9,9′-dioctylfluorene-*co*-benzothiadiazole) (F8BT) and poly(9,9′-dioctylfluorene-*co*-bis-*N*,*N*′-(4-butylphenyl)-bis-*N*,*N*′-phenyl-1,4-phenylenediamine) (PFB) polymers prepared on ITO/PEDOT:PSS and aluminum substrates. Over both PFB- and F8BT-rich domains, the photopotential spectra were found to be proportional to a linear combination of the polymers' absorption spectra. Charge trapping in the film was studied using photopotential fluctuation spectroscopy, in which low-frequency photoinduced electrostatic potential fluctuations were measured by observing noise in the oscillation frequency of a nearby charged atomic force microscope cantilever. Over both F8BT- and PFB-rich regions, the magnitude, distance dependence, frequency dependence, and illumination wavelength dependence of the observed cantilever frequency noise are consistent with photopotential fluctuations arising from stochastic light-driven trapping and detrapping of charges in F8BT. Taken together, our findings suggest a microscopic mechanism by which intermixing of phases leads to charge trapping and thereby to suppressed open-circuit voltage and decreased efficiency in this prototypical bulk heterojunction solar cell film.

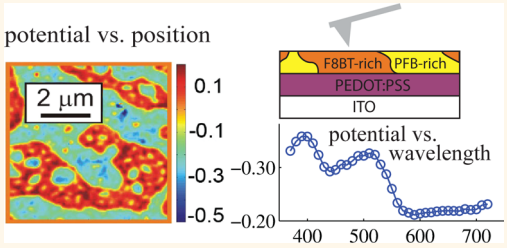


**KEYWORDS:** PFB:P8BT solar cell · open-circuit voltage · scanning Kelvin probe microscopy · photovoltage spectroscopy · photopotential fluctuation spectroscopy

The highest efficiency organic solar cells demonstrated to date employ bulk heterojunctions created in phase-separated blends of conjugated polymers[1−3] or in blends of conjugated polymers and small molecules.[1,2,4] Optimizing vertical[5] and lateral[6] morphology of such bulk heterojunction solar cells is critical to achieving high device efficiency, yet detailed design rules for organic solar cells are still being debated and researched.[2,7−17] Validating solar cell design principles through independent microscopic measurements of the structure and function of bulk heterojunction films has been challenging.[3] Scanning probe microscopy has proved to be a valuable tool for the imaging of device *function* at submicrometer resolution.[6,18] Scanning Kelvin probe microscopy, for example, has been used to image photovoltage;[19−22] time-resolved electric force microscopy has been used to study charge generation;[21,23,24] and photoconductive atomic force[6,15,25−30] and scanning photocurrent microscopy[31,32] have been used to visualize transport networks. In addition, Raman microscopy,[33] fluorescence microscopy,[33] electron microscopy,[33] and X-ray spectromicroscopy[34] have been used to image the structure of blends and determine the phase composition. Near-field scanning optical microscopy has been used to image exciton quenching and thereby map charge-carrier generation efficiency.[35]

Here we study a poly(9,9′-dioctylfluorene-*co*-bis-*N*,*N*′-(4-butylphenyl)-bis-*N*,*N*′-phenyl-1,4-phenylenediamine) and poly(9,9′-dioctylfluorene-*co*-benzothiadiazole) (PFB:F8BT) film—a prototypical bulk heterojunction solar cell material. Initial studies of device performance, luminescence, and topography as a function of blend ratio indicated that charge was generated at the interfaces between micrometer-scale PFB- and F8BT-rich domains in this film.[36] This conclusion was corroborated by an early scanning Kelvin probe microscopy study of photovoltage.[19] Subsequent work has called into question the simple picture that charge is generated at the apparent phase boundaries. Time-resolved electrostatic force microscopy[23] and photocurrent microscopy[32,37] studies indicate that the majority of the photocurrent is instead generated in the

* Address correspondence to jam99@cornell.edu.

Received for review March 2, 2012 and accepted October 2, 2012.

**Published online October 02, 2012**
**10.1021/nn300941f**

center of the PFB- and F8BT-rich domains. X-ray microscopy studies[34] of PFB:F8BT films indicate significant intermixing of PFB and F8BT; the PFB-rich domain contains approximately 30% F8BT, while the F8BT-rich domain contains 10% or less PFB. These findings led us to re-examine the surface photovoltage over a PFB:F8BT film. Here we use wavelength-selective illumination in conjunction with frequency-shift electric force microscopy to acquire spatially resolved *surface photovoltage spectra* over a solar cell film. We find that over both PFB- and F8BT-rich regions, the surface photopotential spectra are a linear combination of the two polymers' absorption spectra.

Here we introduce the use of cantilever frequency noise measurements to probe voltage fluctuations arising from photoinduced carriers. We find that the observed cantilever frequency noise spectra as a function of irradiation wavelength, height, frequency, and tip voltage are quantitatively described by a charge trapping and detrapping model with the charge trap density as a single free parameter. Remarkably, the resulting *voltage-fluctuation spectra* show a wavelength dependence distinct from the surface photopotential data. In both phases, the fluctuation spectra track the absorption spectrum of F8BT, which demonstrates that F8BT absorption generates trap-clearing photocarriers in *both* PFB-rich and F8BT-rich regions. Taken together, our findings indicate that the minority F8BT component in the PFB-rich regions leads to photopotential that does not result from transfer of free carriers but rather from trapped charge—a general efficiency-loss mechanism only briefly considered in previous analyses of intermixing.[19,36−38]

## RESULTS

**Photopotential Experiments.** A PFB(donor):F8BT(acceptor) blend film with a 50:50 composition ratio was fabricated on a PEDOT:PSS/ITO bottom contact as described in the Materials and Methods section. Surface potential and photopotential measurements were carried out using frequency-shift electric force microscopy as described in the Materials and Methods section. Images of surface potential were acquired in the dark and under illumination, with the wavelength of the incident radiation stepped from 350 to 750 nm in 10 nm steps. Figure 1 displays images of surface potential $\phi$ at representative irradiation wavelengths $\lambda$. A topographic image and bulk optical absorption spectra are shown for comparison.

Histograms of surface potential (Figure 1c) show a bimodal distribution corresponding to PFB-rich and F8BT-rich regions. By comparing surface potential images acquired over samples of various PFB:F8BT ratios, we assign the low potential areas in Figure 1b to F8BT-rich regions and the high potential areas to PFB-rich regions (Supporting Information Figure S3). Surface potential images in the dark are shown over ITO/PEDOT:PSS and over Al in Supporting Information

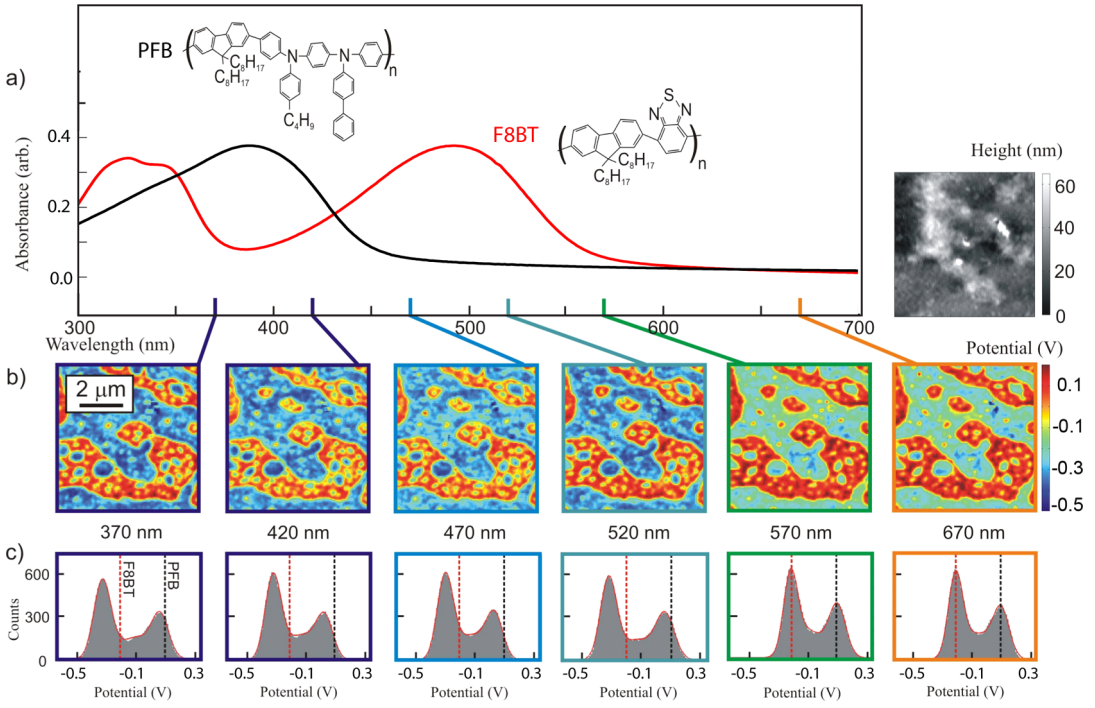


**Figure 1. Wavelength-resolved surface potentiometry of a PFB:F8BT film. (a) Normalized absorption spectra of PFB and F8BT. (b) Maps of surface potential $\phi$ at various wavelengths. The top inset shows the surface topography of the film. (c) Histograms of the surface photopotential maps in (b). Each histogram was fit to a sum of three Gaussians. The best-fit line is shown in red. For comparison, vertical dotted lines have been drawn at the best-fit dark potential for the F8BT-rich regions ($\phi_{dark} = -0.22$ V) and the PFB-rich regions ($\phi_{dark} = 0.10$ V). Parameters: tip−sample separation $d = 90$ nm and cantilever zero-to-peak amplitude $z_{0p} = 30$ nm.**

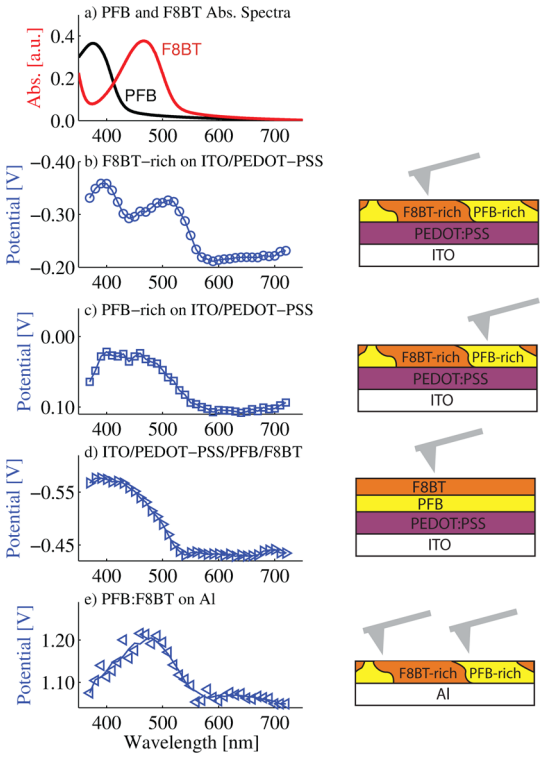


**Figure 2. Mean contact potential and optical absorption *versus* illumination wavelength. (a) Optical absorption spectra of PFB (black; left) and F8BT (red; right) thin films. Surface photopotential spectra over PFB:F8BT films prepared on ITO/PEDOT-PSS: (b) photopotential spectrum of F8BT-rich regions (open circles) and (c) photopotential spectrum of PFB-rich regions (open squares); (d) photopotential spectrum over an F8BT/PFB bilayer film (right-pointing triangles); and (e) surface photopotential spectrum of a PFB:F8BT bulk heterojunction film prepared on an aluminum substrate (left-pointing triangles). We provide inset figures to indicate whether donor-rich or acceptor-rich material is being measured. The *y*-axis has been inverted in (b–d) to facilitate comparing photopotential and absorption spectra. In the case of the aluminum substrate, (e), there is no contact potential contrast between the domains (Supporting Information Figure S7) and the *y*-axis has not been inverted.**

Figure S5. The left and right vertical lines in Figure 1c indicate the average potential of the F8BT-rich and PFB-rich regions, respectively, in the dark. A comparison of the potential in the dark and under illumination shows that light induces a negative shift in the contact potential in both the F8BT-rich and the PFB-rich phases.

To quantify the change in surface potential with illumination wavelength, the histograms of Figure 1c were each fit to a sum of three Gaussians to represent F8BT-rich, PFB-rich, and interfacial regions. The extracted mean potential over the F8BT-rich and PFB-rich regions is plotted *versus* wavelength in Figure 2b,c. F8BT and PFB absorption spectra are plotted for comparison. A bilayer control sample was also prepared *via* spin-coating and lamination.[39] This sample's photopotential decreased upon illumination (Figure 2d), changing monotonically as $\lambda$ passes through the F8BT and

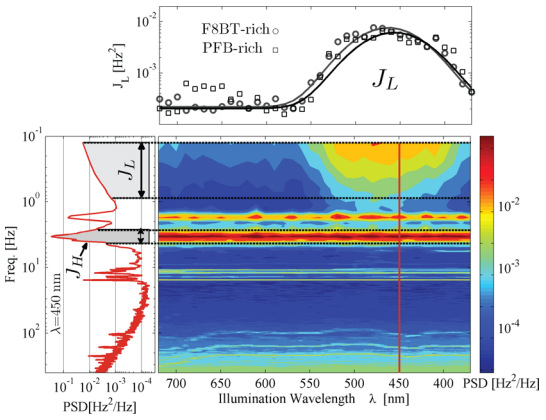


**Figure 3. Left: Power spectral density (PSD) of cantilever frequency fluctuations, $P_{\delta f_c}(f)$, *versus* frequency, *f*, recorded over an F8BT-rich region while illuminated at 450 nm. The shaded areas indicate the low-frequency (0.125 to 0.876 Hz) and high-frequency (2.63 to 4.25 Hz) fluctuations, $J_L$ and $J_H$, respectively. Bottom-right: $P_{\delta f_c}$ *versus* frequency and illumination wavelength over F8BT. Top: Low-frequency fluctuations, $J_L$, as a function of illumination wavelength over F8BT-rich regions (circles). Also included are the low-frequency fluctuations, $J_L$, over PFB-rich regions (squares). The spectral density of the fluctuations over PFB are shown in Supporting Information Figure S17. Parameters: $d$ = 90 nm, $z_{0p}$ = 15 nm, $V_{ts} + \phi$ = 5 V, and $N_{avg}$ = 30.**

PFB absorption maxima. Samples of PFB:F8BT on aluminum showed a photopotential spectrum (Figure 2e) that exactly tracks the F8BT absorption with a *positive* change in contact potential.

**Fluctuation Experiments.** We have carried out spectroscopic measurements of surface photopotential *fluctuations*. In these experiments, the cantilever was driven into self-oscillation *via* positive feedback, and its instantaneous resonance frequency was recorded with submillisecond temporal resolution using a software frequency demodulator as described in the Materials and Methods section. An instantaneous cantilever frequency deviation was computed, $\delta f_c(t) = f_c(t) - f_c$, and a one-sided power spectrum of cantilever frequency fluctuations calculated from

$$P_{\delta f_c}(f) = \int_0^\infty dt\, \cos(2\pi f t)\langle \delta f_c(t)\delta f_c(0)\rangle \qquad (1)$$

Power spectra of cantilever frequency fluctuations over an F8BT-rich region were recorded as a function of irradiation wavelength. The resulting spectra exhibit low-frequency fluctuations ("$J_L$" in Figure 3) showing a strong wavelength dependence and higher-frequency fluctuations ("$J_H$" in Figure 3) which are essentially wavelength-independent. We demonstrate below that the low-frequency fluctuations $J_L$ arise from the voltage fluctuations in the sample while the higher-frequency fluctuations $J_H$ are caused by sample vibrations.[40] The frequency fluctuations above 10 Hz arise from detector noise[40–42] and will not be discussed further.

To study the dependence of cantilever frequency fluctuations on irradiation wavelength, tip voltage, and

distance, we will find it convenient to display an integrated frequency noise or "jitter":

$$J \equiv \int_{f_l}^{f_u} P_{\delta f_c}(f)\mathrm{d}f \qquad (2)$$

where $f_l$ and $f_u$ are the lower and upper frequency cutoffs, respectively. To capture the low-frequency fluctuations in Figure 3, we set $f_l = 0.125$ Hz and $f_u = 0.876$ Hz and call the integrated frequency noise $J_L$. To capture the jitter associated with higher-frequency fluctuations, $J_H$, we set $f_l = 2.6$ Hz and $f_u = 4.2$ Hz. Under single-wavelength illumination, $J_H$ is found to be proportional to $V_{ts}^4$, while $J_L$ is proportional to $V_{ts}^2$ (Supporting Information Figure S14). Since jitter is a function of the difference between tip voltage and contact potential, great care was taken to determine $\phi$ at each wavelength in Figure 3 and to adjust the tip voltage accordingly to keep $V_{ts} - \phi = 5$ V.

In addition to measuring the dependence of frequency fluctuations on tip voltage, we also examined the dependence on the wavelength of illuminated light. In Figure 3, we display frequency fluctuations *versus* wavelength and frequency over an F8BT-rich region. Corresponding data acquired over a PFB-rich region are shown in Supporting Information Figure S17. The high-frequency jitter, indicated by $J_H$ and the dashed lines, is wavelength-independent. The low-frequency jitter, $J_L$, in contrast, is strongly dependent on wavelength; near its peak at 460 nm, $J_L$ in Figure 3 (left) is more than a factor of 30 above the background. The wavelength dependence of the low-frequency jitter $J_L$ over *both* the F8BT-rich and the PFB-rich regions is well described by a single Gaussian with a width of approximately 35 nm and a center wavelength over F8BT-rich and PFB-rich regions of $\lambda_c^{F8BT} = 457 \pm 7$ nm and $\lambda_c^{PFB} = 463 \pm 4$ nm, respectively. These peaks in the jitter spectrum correspond precisely to the low-energy peak in the absorption spectrum of F8BT. The observed jitter depends linearly on light intensity at low power and saturates at high power (Supporting Information Figure S15).

## DISCUSSION

**Photopotential Spectra.** The energy levels of ITO, PEDOT:PSS, PFB, F8BT, and Al are summarized in Figure 4a.[12,43] In the dark, the observed surface potential is lower over F8BT-rich regions than over PFB-rich regions (Figure 1). If the apparent phase boundary behaved as an ideal lateral *pn* junction, with PFB serving as a *p*-type semiconductor and F8BT serving as an *n*-type semiconductor, then one would expect $\phi_{dark}^{F8BT} > \phi_{dark}^{PFB}$. This is just the opposite of what we observe. The interfacial electric field associated with the observed potential step in the dark is oriented to drive photogenerated electrons toward PFB-rich regions and not toward F8BT-rich regions as intended.

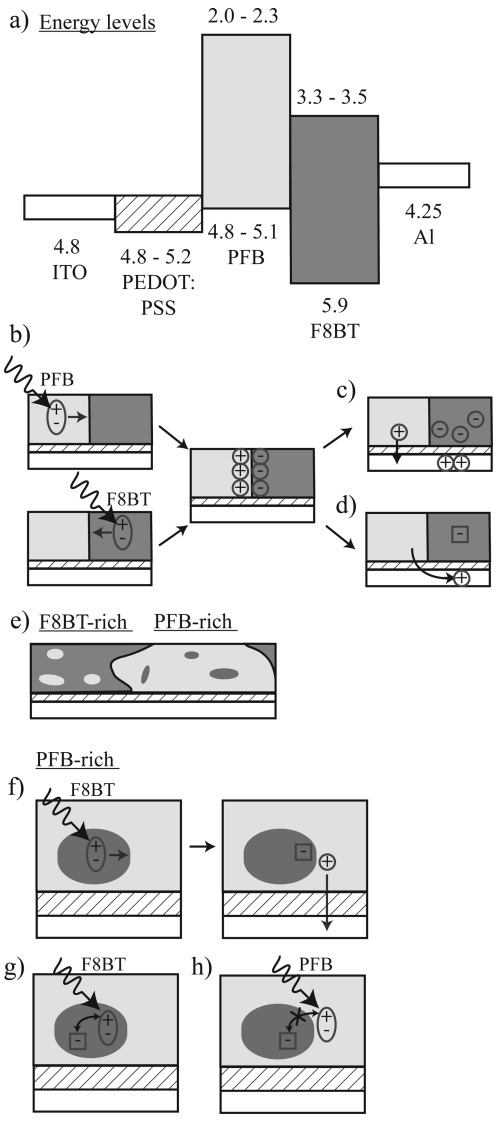


**Figure 4. ITO/PEDOT:PSS/PFB:F8BT under illumination. (a) Energy level diagram of ITO/PEDOT:PSS/PFB:F8BT/Al. (b) We first consider pure phases of PFB and F8BT in contact with one another. Excitons (ovals) generated by light absorption in either PFB (light gray) or F8BT (darker gray) lead to separated charges (circles) at the interface. (c) Scenario in which an electron excess is generated in the F8BT phase due to a disparity in the electron and hole extraction rates. Image charges and image dipoles have been omitted for clarity. (d) Alternative scenario in which an excess of electrons in F8BT arises due to trapped electrons (squares) in the F8BT phase. (e) Sketch of a bulk heterojunction containing phases of mixed composition. (f) Photoexcitation of a minority F8BT inclusion in the PFB-rich phase. Photoinduced detrapping (and subsequent retrapping; not shown) of electrons in F8BT inclusions is facilitated by photoexcitation of (g) F8BT but not (h) PFB.**

The surface potential contrast between F8BT-rich and PFB-rich regions vanishes if the PFB:F8BT film is prepared on an Al substrate (presumably $AlO_x$ or $Al_2O_3$, considering that Al forms a native oxide quickly; Supporting Information Figure S7). Aluminum's native oxide should serve as a tunneling barrier[44] between the organic film and the underlying aluminum. The lack of surface potential contrast on Al thus indicates that

the surface potential variation observed in the dark over ITO/PEDOT:PSS arises from substrate-induced electron/hole doping of the PFB:F8BT film and not from impurities in the constituent polymers. A similar substrate-dependent surface potential has been reported in polymer–fullerene films and interpreted analogously.[20]

Let us now explain the negative sign of the photopotentials seen in Figure 2b,c. The uniformly negative photopotential seen in the figure indicates an excess of photoelectrons in both phases. We first consider pure phases of PFB and F8BT in contact with one another. As sketched in Figure 4b, light absorption in either PFB or F8BT generates excitons which diffuse to the interface and dissociate into free carriers. In the F8BT phase, such an electron excess may be explained as arising from a disparity in the electron and hole extractions rates in F8BT and PFB, respectively. This disparity may arise due to the electron blocking character of the PEDOT:PSS layer,[45,46] as shown in Figure 4c. However, the scenario in Figure 4c is somewhat unlikely since, by some standards, PEDOT:PSS is a poor electron blocker.[45,47] An excess of electrons in F8BT may also arise from trapped electrons, as indicated by the squares in Figure 4d. We note that in scenarios (c) and (d) the negative photopotential in the F8BT phase can arise due to light absorption either in PFB or in F8BT. This finding is consistent with the observation that the photopotential spectrum is a linear combination of the F8BT and PFB absorption spectra. Unfortunately, scenarios (c) and (d) fail to predict the negative sign of the photopotential in the PFB phase. In principle, the negative sign in the photopotential in PFB could arise from electron trapping in PFB. However, such a picture necessitates exciton dissociation in PFB. While there is precedent for exciton dissociation in a pure phase,[37] we see zero photopotential over pure PFB, indicating that exciton dissociation is negligible over pure PFB.

In order to explain the negative sign of the photopotential in PFB, we adopt the explanation of Maturova *et al.* who have observed an analogous net photoinjection of electrons from a substrate into both donor- and acceptor-rich phases under single-wavelength illumination in polymer–fullerene bulk heterojunctions.[20] The authors explained their observations in terms of an intermixing of the donor and acceptor phases. In films composed of PFB and F8BT, such intermixing is well-established.[32,48,49] The PFB-rich domains contain approximately 30% F8BT, while the F8BT-rich domains contain 10% or less PFB.[34] Due to the intermixing of the phases, excitons are dissociated throughout the bulk heterojunction. In Figure 4f, we sketch a mechanism explaining the negative sign of the photopotential in the PFB-rich phase. Light absorption in a minority F8BT inclusion generates excitons which diffuse to the F8BT/PFB interface and create free carriers; photogenerated electrons remain stuck due to either trapping in the minority F8BT inclusions or poor mobility or trapping of electrons in the PFB itself. One possible mechanism of electron trapping is photo-oxidation or electro-oxidation of the fluorene moeity present in both F8BT and PFB polymers.[21,50–52] Consistent with the hypothesis of electron trapping in F8BT, we observe a slow (tens of seconds) decay of the photopotential over F8BT-rich regions (Supporting Information Figure S8); slow decay over PFB-rich regions has been noted previously.[19]

Our photopotential spectra reveal interesting details apparent in neither the Maturova *et al.* scanning Kelvin probe experiment,[20] which employed white-light illumination, nor in the Brenner *et al.* photocurrent microscopy experiments, carried out at selected wavelengths.[32] Control samples of pure F8BT and PFB on ITO/PEDOT:PSS showed no significant surface photopotential in the observed wavelength range (Supporting Information Figure S6), proving that the photopotential observed here is not due to internal photoemission from the substrate. Since PFB also absorbs at long wavelengths, it is plausible that the negative photopotential in our sample could arise from negatively charged PFB degradation products instead. The photovoltage spectrum of Figure 2c, which shows a large photopotential at the peak F8BT absorption, rules out this alternative hypothesis. Brenner *et al.*[32] found that predominantly F8BT domains contributed to *photocurrent* generation. In contrast, on ITO/PEDOT:PSS, we find that F8BT absorption and PFB absorption contribute essentially equally to *photopotential* generation in both phases (Figure 2b,c).

The photopotential spectrum of the PFB:F8BT film prepared on Al/$AlO_x$ indicates a net transfer of electrons toward the Al substrate (Figure 2e); the alternative explanation that the positive photopotential results from vertical charge transfer within the films seems unlikely given the spatial homogeneity of the observed photopotential. It is plausible that photogenerated electrons in the lowest unoccupied molecular orbitals of F8BT and PFB have enough energy to surmount the expected $Al_2O_3$ tunneling barrier and undergo electron transfer to aluminum, so this finding is not inconsistent with the lack of potential contrast observed in the dark over the aluminum substrate. Interestingly, only F8BT absorption contributes to the photopotential on Al/$AlO_x$. This may be because splitting a PFB exciton requires a certain concentration of background charge which is absent in the PFB:F8BT film prepared on Al/$AlO_x$ (Supporting Information Figure S7).

**Fluctuation Spectra.** Fluctuations in the contact potential lead to noise in the cantilever resonance frequency. The frequency noise can be written in terms of $P_{\delta\phi(z_1),\delta\phi(z_2)}$, the power spectrum of the time-domain correlation function $\langle\delta\phi(z_1,t)\delta\phi(z_2,t)\rangle$ of the sample's electrostatic potential at a given height ($d = z_1 = z_2$) and lateral position. At large tip–sample separations $d$,

the cantilever tip can be modeled as a cone, whereas at close separations, it is better approximated as a sphere.[53] For a sphere, the frequency noise is given by[40]

$$P^{\text{sphere}}_{\delta f_c}(f,d) = \frac{f_c^2(V_{ts}-\phi)^2}{4k_c^2}\partial_{z_1}^2\partial_{z_2}^2 \times [C(z_1)C(z_2)P_{\delta\phi(z_1),\delta\phi(z_2)}(f)]|_{d=z_1=z_2} \quad (3)$$

with $f_c$ and $k_c$ being the cantilever resonance frequency and spring constant, respectively, $C$ the tip−sample capacitance, $V_{ts}$ the voltage applied between the tip and the sample, and $\phi$ the sample's local surface potential. The treatment of the case where the cantilever tip is modeled as a cone is presented in the Supporting Information. In both cases, the cantilever frequency noise induced by contact potential fluctuations is quadratic in tip voltage.

External mechanical vibrations will also lead to cantilever frequency fluctuations but will depend quartically on tip voltage.[40] The quartic voltage dependence of the high frequency noise $J_H$, as shown in Supporting Information Figure S14, indicates that $J_H$ is due to mechanical vibrations. This conclusion is corroborated by the fact that $J_H$ in Figure 3 is independent of the illumination wavelength $\lambda$. The absence of a systematic dependence of $J_H$ on $\lambda$ demonstrates that the wavelength dependence of $J_L$ is not due to a failure to accurately track $\phi$. As shown in Supporting Information Figure S14 $J_L$ depends quadratically on $V_{ts}$, consistent with eq 3. The quadratic dependence of $J_L$ on $V_{ts}$ indicates that the cantilever tip is passively observing the sample's electrostatic potential fluctuations, as assumed in eq 3. Control experiments also show that $J_L$ is due to neither photoinduced changes in the tip sample capacitance (Supporting Information Figure S10) nor fluctuations in the intensity of the light source (Supporting Information Figure S12).

Comparing the jitter *versus* illumination wavelength spectra in Figure 3 to the absorption spectra in Figure 1, we conclude that photovoltage fluctuations $J_L$ are induced by light absorption in F8BT exclusively. In contrast, Brenner *et al.*[32] found that while photocurrent over both PFB-rich and F8BT-rich domains arose primarily from F8BT absorption, the PFB absorption contribution to photocurrent was nevertheless substantial.

Previous work on F8BT:PFB solar cells has suggested the presence of trapped states, which manifest themselves as a slow decay of the potential in the dark.[19] We likewise observe a slow decay of photopotential over F8BT-rich regions in our sample (Supporting Information Figure S8), consistent with slow release of trapped electrons or, alternatively but less likely, slow recombination of electrons with holes in the substrate. Here we develop a mathematical model describing how trapped states under illumination lead to fluctuations in the surface potential.

We compute $P^{\text{single}}_{\phi_1,\phi_2}(f)$, the cross-correlation function of the electrostatic potential in eq 3, from stochastic charge trapping and detrapping at localized sites. The power spectrum of electrostatic potential fluctuations arising from a single trapping site is that of a random telegraph signal and is given by[54]

$$P^{\text{single}}_{\phi_1,\phi_2}(f) = \frac{4\phi_1\phi_2}{(\tau_f+\tau_v)(\tau^{-2}+4\pi^2f^2)} \quad (4)$$

where $\phi_i = \phi(\mathbf{r},z_i)$ is the electric potential due to a filled trap, $\tau_f^{-1}$ and $\tau_v^{-1}$ are the rates associated with trapping and detrapping, respectively, and $\tau^{-1} = \tau_f^{-1} + \tau_v^{-1}$. Let us assume that the trapping and detrapping rates follow the Arrhenius law, that is, $\tau_i^{-1} \propto e^{-E/k_BT}$, and let us further assume that there is not a single energy barrier $E$ but a flat distribution of barriers between $E_{low}$ and $E_{high}$ whose rates bracket the observed frequency range: $\tau_{low}^{-1} \ll f \ll \tau_{high}^{-1}$. For a trapping site density per unit area of $\sigma$, the fluctuation in potential due to all of the trapping sites in the film is

$$P_{\phi_1,\phi_2}(f) = \frac{1}{E_{high}-E_{low}}\int_{E_{low}}^{E_{high}} dE \times\sigma\int d\mathbf{r}P^{\text{single}}_{\phi_1,\phi_2}(f) \quad (5)$$

Performing the integral over energies, we find that the fluctuations in potential can be written as

$$P_{\phi_1,\phi_2}(f) = \frac{4\pi c_{trap}k_BT}{2f(E_{high}-E_{low})}\int d\mathbf{r}\phi_2\phi_1 \quad (6)$$

where $c_{trap} \equiv \beta(1-\beta)\sigma$ and $\beta = \tau_f/(\tau_f+\tau_v)$ is the fraction of the traps that are occupied. Assuming that the trapping sites lie below the Fermi energy, most traps are occupied (*i.e.*, $\beta \approx 1$) and we can take $c_{trap}$ to be the number of vacant traps per unit area (*i.e.*, $c_{trap} \approx (1-\beta)\sigma$). To avoid a divergence of the voltage fluctuations, we find it necessary to modify the potential $\delta\phi(\mathbf{r},z)$ in eq 6 to include the image potential associated with counter charges present in the underlying ITO/PEDOT:PSS substrate. Including effects of image charges, we find from eqs 3 and 6 that the induced frequency noise for the sphere model can be approximated by

$$P^{\text{trapping}}_{\delta f_c}(f,d) = \frac{\pi^2c_{trap}f_c^2C^2(V_{ts}-\phi)^2k_BT}{k_c^2(E_{high}-E_{low})f}\left(\frac{q}{4\pi\varepsilon_0}\right)^2 J_4\left(d,\frac{2h}{\varepsilon_r}\right) \quad (7)$$

with

$$J_n(d,\Delta) = (n-1)![(2d)^{-n} - 2(2d+\Delta)^{-n} + (2d+2\Delta)^{-n}] \quad (8)$$

where $h$ is the thickness of the film. In the Supporting Information, we have derived a similar expression for frequency for a conical, rather than a spherical, cantilever tip.

We found that a trap density per unit energy of $c_{trap}/(E_{high}-E_{low}) = 10^{13}$ m$^{-2}$ eV$^{-1}$ is consistent with

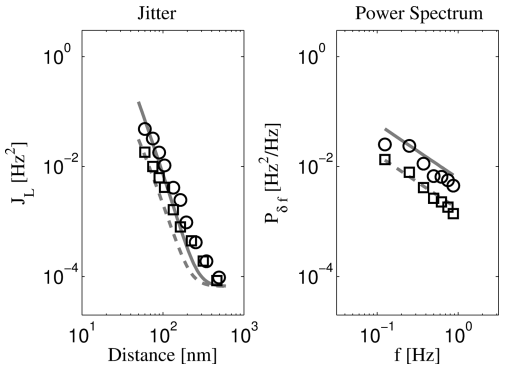


**Figure 5. Comparison of observed and calculated low-frequency jitter $J_L$ *versus* $d$ (left) and the power spectrum $P_{\delta f_c}$ *versus* $f$ at $d$ = 90 nm (right). The data were acquired over an F8BT-rich region (circles) and a PFB-rich region (squares). The prediction from the trapping and detrapping model is shown for the case of charges distributed at the top of the film (eq 7; solid gray line) and throughout the volume of the film (eq 9 in the Supporting Information; dashed gray line). A vacant trap density per unit energy of $c_{trap}/(E_{high} - E_{low})$ = $10^{13}$m$^{-2}$ eV$^{-1}$ was used for this calculation.**

the magnitude of the observed frequency noise. Using a trap bandwidth of $E_{high} - E_{low}$ = 0.125 eV,[55] we find that the corresponding vacant trap density is $c_{trap}$ = $1.25 \times 10^{12}$ m$^{-2}$. Trapping throughout the film volume was also modeled by integrating eq 7 over the film (thickness $t$ = 200 nm, dielectric constant $\varepsilon = 3\varepsilon_0$). The sphere radius and cone angle were taken to be 40 nm and 20°, respectively. The sphere and cone capacitance were calculated as in refs 42 and 53. We can see in Figure 5 that the distance dependence and the frequency dependence of the cantilever frequency fluctuations are correctly predicted for both a uniform distribution of charges throughout the film and for charges distributed at the top of the film.

In order to compare the density $c_{trap}$ necessary to reproduce the data to the density of photoinduced charge $\Delta\sigma_{light}$, we modeled F8BT/PFB as a uniformly charged film with a sheet of counter charge present in the underlying ITO/PEDOT:PSS. In this approximation, the concentration of photoinduced charge is related to the observed photopotential $\Delta\phi_{light}$ by $\Delta\rho_{light}$ = $2\varepsilon_s\Delta\phi_{light}/q_e t^2$, with $t$ = 200 nm as the sample thickness, $\varepsilon_s$ the sample dielectric constant, and $q_e$ the charge of the carrier. Taking $\varepsilon_s = 3\varepsilon_0$ and $\Delta\phi_{light}$ = 0.15 V, we estimate $\Delta\rho_{light} \approx 1.2 \times 10^{21}$ m$^{-3}$. The corresponding planar density of photoinduced charrge is $\Delta\sigma_{light} = \Delta\rho_{light} t = 2.5 \times 10^{14}$ m$^{-2}$ and corresponds with estimates from literature.[20] From this estimate, we conclude that the fraction $\beta$ of traps that are occupied is ≈0.995.

Having established charge trapping and detrapping as a plausible explanation for frequency noise, we now discuss the details of the trapping mechanism. It is observed that over both F8BT-rich and PFB-rich regions the spectral shape of the frequency fluctuations in Figure 3 track the absorption of F8BT exclusively, indicating that the noise in both regions arises from traps populated and depopulated by photocarriers generated by F8BT absorption. Electron traps agree with the qualitative picture in Figure 4 and seem to us a more reasonable hypothesis than hole traps. Figure 4g,h illustrates how illumination of F8BT, but not PFB, results in photoinduced trapping and detrapping. The key hypothesis is that electrons are trapped in F8BT—in PFB-rich regions, these trapped electrons are cleared by recombination with an F8BT exciton; a PFB exciton simply cannot get into close enough proximity to clear the trapped electrons in the F8BT inclusions. The spectra of Figure 3 indicate that the concentration of trapped electrons in F8BT is roughly equal in both the PFB-rich and F8BT-rich domains over ITO/PEDOT:PSS.

Frequency noise was not observed over the PFB:F8BT sample prepared on Al/$AlO_x$ (Supporting Information Figure S13). One explanation is that, under illumination, Al/$AlO_x$ is enough of an electron sink to lower the electron concentration and suppress electron trapping and detrapping at F8BT sites in the PFB-rich region. A second explanation is that electron traps arise in F8BT in the PFB-rich regions due to substrate-induced electron/hole doping, which is clearly much lower over Al/$AlO_x$ than over ITO/PEDOT:PSS.

## CONCLUSIONS

A key parameter determining the efficiency of any solar cell is the open-circuit voltage. In organic bulk heterojunction solar cells, the open-circuit voltage is determined by the energy levels of the constituent molecules[7,11] but is also thought to depend critically on photoinduced carrier concentration gradients,[8] electric-field and disorder-dependent geminate separation[9,56] and recombination,[10,12,14,16] nanostructure and morphology,[15] shunt resistance,[57] and reverse saturation current.[13] Scanning probe measurements of contact potential and current have been used to infer the role of morphology in determining open-circuit voltage;[15,19,27] however, these studies did not systematically vary the wavelength of the illuminating light. Here we have introduced surface photopotential spectroscopy and photopotential fluctuation spectroscopy as two complementary tools for probing the fate of photogenerated charges in a bulk heterojunction solar cell film and for investigating mechanisms of open-circuit losses in bulk heterojunction solar cells.

While surface photopotential spectroscopy has proved a powerful tool for studying the sign and dynamics of photoinduced carriers in inorganic semiconductors,[58,59] there is little precedent for acquiring surface photopotential spectra of organic semiconductors[60,61] and no precedent for acquiring variable wavelength contact potential images of organic semiconductor films. Much prior work has been done to understand *photocurrent* generation in PFB:F8BT films. Here we have demonstrated that both PFB and F8BT contribute

essentially equally to the observed *photopotential* over both PFB- and F8BT-rich regions.

From experiments of photopotential fluctuations *versus* illumination wavelength, frequency, tip–sample distance, and applied tip voltage, we have inferred a local spatial density of electron traps in F8BT. Bulk voltage-noise measurements have been used to study trapping–detrapping fluctuations[62] and percolation transport[63] in organic semiconductor films, while cantilever frequency noise has been used to study charge blinking,[64] generation-recombination noise in inorganic semiconductor heterojunctions,[65] and dielectric fluctuations in thin polymer films.[40,42,66] Here we have demonstrated that photoinduced voltage fluctuations can exhibit a characteristic dependence on illumination wavelength and can be understood quantitatively.

Scanning Kelvin probe microscopy data are necessarily acquired on films prepared with the top cathode absent. Because of this limitation, Maturova *et al.* have cautioned that numerical modeling of charge transport is probably required to draw conclusions relevant to solar cell operation from SPKM data.[20] We indeed find that the potential in the dark and under illumination in PFB:F8BT is different over ITO/PEDOT:PSS and Al/$AlO_x$ substrates. While we agree that numerical modeling could provide even more insight into PFB:F8BT solar cell operation, we find that we can explain our results qualitatively in a self-consistent way that yields useful new information. Our data indicate that poor connectivity of F8BT in the PFB-rich regions in the ITO/PEDOT:PSS/PFB:F8BT sample leads to a buildup of negative charge in PFB-rich regions under illumination and an accompanying loss of open-circuit voltage. Since the adjacent F8BT-rich region already provides an electron sink, we would expect this problem to persist even with the top cathode present. Solar cells made from patterned donors and acceptors,[67] block copolymers,[68] and covalent organic frameworks[69] would not suffer from this proposed photovoltage loss mechanism.

## MATERIALS AND METHODS

**Sample Preparation.** Solar cells were fabricated from a 1:1 (unless otherwise noted) solution of PFB (poly[(9,9-dioctylfluorenyl-2,7-diyl)-*co*-(*N*,*N*′-diphenyl)-*N*,*N*′-di(butylphenyl)-1,4-diamino benzene]) and F8BT (poly[(9,9-dioctylfluorenyl-2,7-diyl)-*alt*-*co*-(1,4-benzo-2,1′,3-thiadiazole)]) (American Dye Source, ADS232GE and ADS133YE, respectively).

In order to minimize photo-oxidation, which can lead to the formation of electron trapping fluorenone defects,[21,50–52] the solar cell solution was prepared and spin-cast at night under red light illumination. To prepare the solar cell films, the PFB and F8BT were dissolved in anhydrous *p*-xylene (Sigma-Aldrich, used as received), sonicated for 40 min, and heated at 50 °C. The 200 nm thick films studied here were made from a solution of 30 mg of PFB and 30 mg of F8BT dissolved in 2.5 mL of *p*-xylene. A PEDOT:PSS (Clevios PH500) layer was deposited on bare ITO (KinTec, unpatterned) by spin-coating for 60 s at 6000 rpm (approximately 25 nm thickness). The PEDOT:PSS layer was annealed at 170 °C for 2 min in atmosphere before the substrates were transferred to a glovebox where the PFB:F8BT solution was applied by spin-coating for 60 s at 2000 rpm. Films were then annealed at 160 °C for 5 min in a glovebox. Bilayer devices were fabricated *via* the method described in ref 39. Samples were transferred to the scanning probe microscope at night and under red light illumination in order to minimize photo-oxidation; samples were exposed to air for less than 10 min during transfer. It is known that exposure to air and light on the order of days does not affect surface photopotential.[21]

The absorption spectra shown in Figure 1a and Figure 2a were collected as follows. The homopolymer samples were prepared by spin-casting a solution containing 20 mg of the polymer (PFB or F8BT) in 1 mL of *p*-xylene at 3000 rpm for 60 s onto fused silica substrates. The resulting films were 55 nm (PFB) and 45 nm (F8BT) thick. The absorption spectra were measured using a UV–vis spectrometer (Varian Cary 5000) with fused silica as the reference.

**Electric Force Microscopy.** Surface potential maps were collected by scanning a metalized cantilever (SPMTips NSC-18; Ti–Pt coated; spring constant $k_c$ = 3.5 N m$^{-1}$, resonance frequency $f_c$ = 65.1 kHz, quality factor $Q \approx 6 \times 10^3$ in vacuum, far away from the sample) across a $6 \times 6$ $\mu$m$^2$ area at a velocity of 4.2 s per line. The position of the cantilever was observed with a temperature-tuned fiber-optic interferometer operating at 1310 nm. The cantilever was driven, *via* positive feedback at fixed drive amplitude, to a zero-to-peak amplitude of 30 nm and scanned at a constant height of 90 nm relative to the mean height of the sample. The location of the sample surface was determined within 3 nm by advancing the cantilever until the cantilever frequency changed by ≥20 Hz due to intermolecular forces. Shifts in cantilever frequency were detected by a frequency demodulator running on a field-programmable gate array (RHK PLLpro; output bandwidth set to 400 Hz). The tip voltage was modulated with a $f_m$ = 160 Hz, 3 V zero-to-peak sine wave. First and second harmonics of the resulting cantilever frequency oscillation were inferred *via* lock-in detection (30 and 50 ms time constant, respectively). The signal at the first harmonic was continuously nulled by applying an additional tip voltage from a commercial proportional-integral-derivative feedback controller ($P$ = OFF, $I$ = 80 Hz, and $D$ = 0.05 ms). The additional tip voltage required to null the (first) harmonic of the cantilever frequency at $f_m$ is equal to the local contact potential $\phi$.

**Sample Illumination.** To illuminate the sample, a tungsten–halogen light source (Ushio EKE) was fiber-coupled (ThorLabs, AFS 50/125Y) to a multimode optical fiber of core diameter 50 $\mu$m and numerical aperture NA = 0.22. The fiber was positioned roughly 200 $\mu$m away from the cantilever tip, inclined at an angle of 30° from horizontal. Visible light was passed through a computer-controlled attenuator, projected at a constant intensity (unless otherwise noted) of 0.015 $\mu$W and a bandwidth of 5 nm onto the multimode fiber core. We estimate the resulting intensity and spectral irradiance at the sample to be 0.03 mW cm$^{-2}$ and 0.006 mW cm$^{-2}$ nm$^{-1}$, respectively.

**Noise Measurements.** The cantilever was oscillated *via* positive feedback with a fixed-amplitude drive to a zero-to-peak amplitude of 15 nm. The tip was held, except where noted, at a mean tip–sample distance of $d$ = 90 nm and at a voltage of 5 V above the local electrostatic potential, $V_{ts} - \phi$ = 5 V. The displacement of the cantilever was observed by fiber-optic interferometry, digitally sampled at 260.0 kHz, and sent to a software frequency demodulator[42] which estimated the instantaneous cantilever frequency at an update rate of 11.82 kHz. The frequency demodulator output was passed through a 20th order Butterworth band-pass filter centered at $f_c$ (bandwidth = 2 × 1000 Hz). Frequency noise power spectra were obtained by Fourier transforming the autocorrelation function of the frequency fluctuations, recorded for 8–10 s typically, and averaging $N_{avg}$ = 30 spectra together. The resulting one-sided power spectrum of cantilever frequency fluctuations was integrated

between ≈0.125 and ≈0.876 Hz to obtain the jitter. An additional 10 s delay was implemented after any change in the illumination wavelength or tip voltage.

*Conflict of Interest:* The authors declare no competing financial interest.

*Acknowledgment.* The authors acknowledge the support of the U.S. National Science Foundation, through Grants DMR-1006633 and DMR-0706508 (J.L.L., R.B., A.R.J., and J.A.M.), and through the Cornell Center for Nanoscale Systems *via* Grants EEC-0117770 and EEC-0646547 (N.H. and J.A.M.). This work was performed in part at the Cornell NanoScale Science and Technology Facility, a member of the National Nanotechnology Infrastructure Network, supported by the National Science Foundation (ECS-0335765). C.G. thanks Prof. David Ginger of the University of Washington and acknowledges the Royal Society for a travel grant as well as the use of facilities supported by grants from the Murdock Foundation and AFOSR, and minor materials support from the U.S. National Science Foundation. The authors thank David Ginger, Swapna Lekkala, and Roger Loring for helpful discussions.

*Supporting Information Available:* Movies illustrating the evolution of the surface-potential maps and histograms during wavelength scanning; device characterization and materials-assignment data; additional photopotential data (pure-phase and Al substrate controls, decay transient, and dependence on light intensity); photocapacitance data; a derivation of jitter for a conical cantilever tip; and additional photopotential fluctuation data (analysis of light-intensity noise; dependence on tip voltage, distance, and light intensity; an Al substrate control; and a detailed analysis of fluctuation power spectra *versus* wavelength, distance, and tip voltage). This material is available free of charge *via* the Internet at http://pubs.acs.org.

## REFERENCES AND NOTES

1. Scharber, M.; Mühlbacher, D.; Koppe, M.; Denk, P.; Waldauf, C.; Heeger, A.; Brabec, C. Design Rules for Donors in Bulk-Heterojunction Solar Cells—Towards 10% Energy-Conversion Efficiency. *Adv. Mater.* **2006**, *18*, 789–794.
2. Dennler, G.; Scharber, M. C.; Ameri, T.; Denk, P.; Forberich, K.; Waldauf, C.; Brabec, C. J. Design Rules for Donors in Bulk-Heterojunction Tandem Solar Cells—Towards 15% Energy-Conversion Efficiency. *Adv. Mater.* **2008**, *20*, 579.
3. McNeill, C. R.; Greenham, N. C. Conjugated-Polymer Blends for Optoelectronics. *Adv. Mater.* **2009**, *21*, 3840–3850.
4. Liang, Y.; Feng, D.; Wu, Y.; Tsai, S.-T.; Li, G.; Ray, C.; Yu, L. Highly Efficient Solar Cell Polymers Developed *via* Fine-Tuning of Structural and Electronic Properties. *J. Am. Chem. Soc.* **2009**, *131*, 7792–7799.
5. Arias, A. C.; Corcoran, N.; Banach, M.; Friend, R. H.; MacKenzie, J. D.; Huck, W. T. S. Vertically Segregated Polymer-Blend Photovoltaic Thin-Film Structures through Surface-Mediated Solution Processing. *Appl. Phys. Lett.* **2002**, *80*, 1695–1697.
6. Groves, C.; Reid, O. G.; Ginger, D. S. Heterogeneity in Polymer Solar Cells: Local Morphology and Performance in Organic Photovoltaics Studied with Scanning Probe Microscopy. *Acc. Chem. Res.* **2010**, *43*, 612–620.
7. Brabec, C. J.; Cravino, A.; Meissner, D.; Sariciftci, N. S.; Fromherz, T.; Rispens, M. T.; Sanchez, L.; Hummelen, J. C. Origin of the Open Circuit Voltage of Plastic Solar Cells. *Adv. Funct. Mater.* **2001**, *11*, 374–380.
8. Gregg, B. A. Excitonic Solar Cells. *J. Phys. Chem. B* **2003**, *107*, 4688–4698.
9. Peumans, P.; Forrest, S. R. Separation of Geminate Charge-Pairs at Donor−Acceptor Interfaces in Disordered Solids. *Chem. Phys. Lett.* **2004**, *398*, 27–31.
10. Koster, L. J. A.; Mihailetchi, V. D.; Ramaker, R.; Blom, P. W. M. Light Intensity Dependence of Open-Circuit Voltage of Polymer:Fullerene Solar Cells. *Appl. Phys. Lett.* **2005**, *86*, 123509.
11. Rand, B. P.; Burk, D. P.; Forrest, S. R. Offset Energies at Organic Semiconductor Heterojunctions and Their Influence on the Open-Circuit Voltage of Thin-Film Solar Cells. *Phys. Rev. B* **2007**, *75*, 115327.
12. Westenhoff, S.; Howard, I. A.; Hodgkiss, J. M.; Kirov, K. R.; Bronstein, H. A.; Williams, C. K.; Greenham, N. C.; Friend, R. H. Charge Recombination in Organic Photovoltaic Devices with High Open-Circuit Voltages. *J. Am. Chem. Soc.* **2008**, *130*, 13653–13658.
13. Potscavage, W. J., Jr.; Sharma, A.; Kippelen, B. Critical Interfaces in Organic Solar Cells and Their Influence on the Open-Circuit Voltage. *Acc. Chem. Res.* **2009**, *42*, 1758–1767.
14. Garcia-Belmonte, G.; Bisquert, J. Open-Circuit Voltage Limit Caused by Recombination through Tail States in Bulk Heterojunction Polymer-Fullerene Solar Cells. *Appl. Phys. Lett.* **2010**, *96*, 113301.
15. Reid, O. G.; Xin, H.; Jenekhe, S. A.; Ginger, D. S. Nanostructure Determines the Intensity-Dependence of Open-Circuit Voltage in Plastic Solar Cells. *J. Appl. Phys.* **2010**, *108*, 084320.
16. Maurano, A.; Hamilton, R.; Shuttle, C. G.; Ballantyne, A. M.; Nelson, J.; O'Regan, B.; Zhang, W.; McCulloch, I.; Azimi, H.; Morana, M.; Brabec, C. J.; Durrant, J. R. Recombination Dynamics as a Key Determinant of Open Circuit Voltage in Organic Bulk Heterojunction Solar Cells: A Comparison of Four Different Donor Polymers. *Adv. Mater.* **2010**, *22*, 4987.
17. Schlenker, C. W.; Thompson, M. E. The Molecular Nature of Photovoltage Losses in Organic Solar Cells. *Chem. Commun.* **2011**, *47*, 3702–3716.
18. Pingree, L. S. C.; Reid, O. G.; Ginger, D. S. Electrical Scanning Probe Microscopy on Active Organic Electronic Devices. *Adv. Mater.* **2009**, *21*, 19–28.
19. Chiesa, M.; Bürgi, L.; Kim, J. S.; Shikler, R.; Friend, R. H.; Sirringhaus, H. Correlation between Surface Photovoltage and Blend Morphology in Polyfluorene-Based Photodiodes. *Nano Lett.* **2005**, *5*, 559–563.
20. Maturova, K.; Kemerink, M.; Wienk, M.; Charrier, D.; Janssen, R. Scanning Kelvin Probe Microscopy on Bulk Heterojunction Polymer Blends. *Adv. Funct. Mater.* **2009**, *19*, 1379–1386.
21. Reid, O. G.; Rayermann, G. E.; Coffey, D. C.; Ginger, D. S. Imaging Local Trap Formation in Conjugated Polymer Solar Cells: A Comparison of Time-Resolved Electrostatic Force Microscopy and Scanning Kelvin Probe Imaging. *J. Phys. Chem. C* **2010**, *114*, 20672–20677.
22. Spadafora, E. J.; Demadrille, R.; Ratier, B.; Grevin, B. Imaging the Carrier Photogeneration in Nanoscale Phase Segregated Organic Heterojunctions by Kelvin Probe Force Microscopy. *Nano Lett.* **2010**, *10*, 3337–3342.
23. Coffey, D. C.; Ginger, D. S. Time-Resolved Electrostatic Force Microscopy of Polymer Solar Cells. *Nat. Mater.* **2006**, *5*, 735–740.
24. Giridharagopal, R.; Rayermann, G. E.; Shao, G.; Moore, D. T.; Reid, O. G.; Tillack, A. F.; Masiello, D. J.; Ginger, D. S. Submicrosecond Time Resolution Atomic Force Microscopy for Probing Nanoscale Dynamics. *Nano Lett.* **2012**, *12*, 893–898.
25. Bull, T. A.; Pingree, L. S. C.; Jenekhe, S. A.; Ginger, D. S.; Luscombe, C. K. The Role of Mesoscopic PCBM Crystallites in Solvent Vapor Annealed Copolymer Solar Cells. *ACS Nano* **2009**, *3*, 627–636.
26. Pingree, L. S. C.; Reid, O. G.; Ginger, D. S. Imaging the Evolution of Nanoscale Photocurrent Collection and Transport Networks during Annealing of Polythiophene/Fullerene Solar Cells. *Nano Lett.* **2009**, *9*, 2946–2952.
27. Dang, X.-D.; Tamayo, A. B.; Seo, J.; Hoven, C. V.; Walker, B.; Nguyen, T.-Q. Nanostructure and Optoelectronic Characterization of Small Molecule Bulk Heterojunction Solar Cells by Photoconductive Atomic Force Microscopy. *Adv. Funct. Mater.* **2010**, *20*, 3314–3321.
28. Hamadani, B. H.; Jung, S.; Haney, P. M.; Richter, L. J.; Zhitenev, N. B. Origin of Nanoscale Variations in Photoresponse of an Organic Solar Cell. *Nano Lett.* **2010**, *10*, 1611–1617.
29. Hamadani, B. H.; Gergel-Hackett, N.; Haney, P. M.; Zhitenev, N. B. Imaging of Nanoscale Charge Transport in Bulk

Heterojunction Solar Cells. *J. Appl. Phys.* **2011**, *109*, 124501.
30. Dang, X.-D.; Mikhailovsky, A.; Nguyen, T.-Q. Measurement of Nanoscale External Quantum Efficiency of Conjugated Polymer:Fullerene Solar Cells by Photoconductive Atomic Force Microscopy. *Appl. Phys. Lett.* **2010**, *97*, 113303.
31. McNeill, C. R.; Dastoor, P. C. Photocurrent Pattern Formation in Polymer/Methanofullerene Blends Imaged by Near-Field Scanning Photocurrent Microscopy. *J. Appl. Phys.* **2006**, *99*, 033502.
32. Brenner, T. J. K.; McNeill, C. R. Spatially Resolved Spectroscopic Mapping of Photocurrent and Photoluminescence in Polymer Blend Photovoltaic Devices. *J. Phys. Chem. C* **2011**, *115*, 19364–19370.
33. Xia, Y.; Friend, R. Phase Separation of Polyfluorene-Based Blend Films and Its Influence on Device Operations. *Adv. Mater.* **2006**, *18*, 1371.
34. McNeill, C. R.; Watts, B.; Thomsen, L.; Ade, H.; Greenham, N. C.; Dastoor, P. C. X-ray Microscopy of Photovoltaic Polyfluorene Blends: Relating Nanomorphology to Device Performance. *Macromolecules* **2007**, *40*, 3263–3270.
35. Cadby, A.; Khalil, G.; Fox, A. M.; Lidzey, D. G. Mapping Exciton Quenching in Photovoltaic-Applicable Polymer Blends Using Time-Resolved Scanning Near-Field Optical Microscopy. *J. Appl. Phys.* **2008**, *103*, 093715.
36. Snaith, H.; Arias, A.; Morteani, A.; Silva, C.; Friend, R. Charge Generation Kinetics and Transport Mechanisms in Blended Polyfluorene Photovoltaic Devices. *Nano Lett.* **2002**, *2*, 1353–1357.
37. McNeill, C. R.; Frohne, H.; Holdsworth, J. L.; Dastoor, P. C. Near-Field Scanning Photocurrent Measurements of Polyfluorene Blend Devices: Directly Correlating Morphology with Current Generation. *Nano Lett.* **2004**, *4*, 2503–2507.
38. Shikler, R.; Chiesa, M.; Friend, R. H. Photovoltaic Performance and Morphology of Polyfluorene Blends: The Influence of Phase Separation Evolution. *Macromolecules* **2006**, *39*, 5393–5399.
39. Ramsdale, C. M.; Barker, J. A.; Arias, A. C.; MacKenzie, J. D.; Friend, R. H.; Greenham, N. C. The Origin of the Open-Circuit Voltage in Polyfluorene-Based Photovoltaic Devices. *J. Appl. Phys.* **2002**, *92*, 4266–4270.
40. Hoepker, N.; Lekkala, S.; Loring, R. F.; Marohn, J. A. Quantifying Dielectric Fluctuations over Polymer Films Using an Atomic Force Microscope. *J. Phys. Chem. B* **2011**, *115*, 14493–14500.
41. Yazdanian, S. M.; Marohn, J. A.; Loring, R. F. Dielectric Fluctuations in Force Microscopy: Noncontact Friction and Frequency Jitter. *J. Chem. Phys.* **2008**, *128*, 224706.
42. Yazdanian, S. M.; Hoepker, N.; Kuehn, S.; Loring, R. F.; Marohn, J. A. Quantifying Electric Field Gradient Fluctuations over Polymers Using Ultrasensitive Cantilevers. *Nano Lett.* **2009**, *9*, 2273–2279.
43. Morteani, A. C.; Sreearunothai, P.; Herz, L. M.; Friend, R. H.; Silva, C. Exciton Regeneration at Polymeric Semiconductor Heterojunctions. *Phys. Rev. Lett.* **2004**, *92*, 247402.
44. Gloos, K.; Koppinen, P. J.; Pekola, J. P. Properties of Native Ultrathin Aluminium Oxide Tunnel Barriers. *J. Phys.: Condens. Matter* **2003**, *15*, 1733–1746.
45. Yan, H.; Scott, B. J.; Huang, Q.; Marks, T. J. Enhanced Polymer Light-Emitting Diode Performance Using a Cross-linked-Network Electron-Blocking Interlayer. *Adv. Mater.* **2004**, *16*, 1948–1953.
46. Koch, N.; Elschner, A.; Johnson, R. L. Green Polyfluorene-Conducting Polymer Interfaces: Energy Level Alignment and Device Performance. *J. Appl. Phys.* **2006**, *100*, 024512.
47. Ratcliff, E. L.; Zacher, B.; Armstrong, N. R. Selective Interlayers and Contacts in Organic Photovoltaic Cells. *J. Phys. Chem. Lett.* **2011**, *2*, 1337–1350.
48. Kietzke, T.; Neher, D.; Kumke, M.; Montenegro, R.; Landfester, K.; Scherf, U. A Nanoparticle Approach To Control the Phase Separation in Polyfluorene Photovoltaic Devices. *Macromolecules* **2004**, *37*, 4882–4890.
49. McNeill, C. R.; Watts, B.; Thomsen, L.; Belcher, W. J.; Greenham, N. C.; Dastoor, P. C. Nanoscale Quantitative Chemical Mapping of Conjugated Polymer Blends. *Nano Lett.* **2006**, *6*, 1202–1206.
50. List, E.; Guentner, R.; de Freitas, P.; Scherf, U. The Effect of Keto Defect Sites on the Emission Properties of Polyfluorene-Type Materials. *Adv. Mater.* **2002**, *14*, 374–378.
51. Scherf, U.; List, E. Semiconducting Polyfluorenes—Towards Reliable Structure–Property Relationships. *Adv. Mater.* **2002**, *14*, 477–487.
52. Bliznyuk, V. N.; Carter, S. A.; Scott, J. C.; Klärner, G.; Miller, R. D.; Miller, D. C. Electrical and Photoinduced Degradation of Polyfluorene Based Films and Light-Emitting Devices. *Macromolecules* **1999**, *32*, 361–369.
53. Cherniavskaya, O.; Chen, L.; Weng, V.; Yuditsky, L.; Brus, L. E. Quantitative Noncontact Electrostatic Force Imaging of Nanocrystal Polarizability. *J. Phys. Chem. B* **2003**, *107*, 1525–1531.
54. Machlup, S. Noise in Semiconductors: Spectrum of a Two-Parameter Random Signal. *J. Appl. Phys.* **1954**, *25*, 341–343.
55. Zhang, Y.; Blom, P. W. M. Electron and Hole Transport in Poly(fluorene-benzothiadiazole). *Appl. Phys. Lett.* **2011**, *98*, 143504.
56. Groves, C.; Marsh, R. A.; Greenham, N. C. Monte Carlo Modeling of Geminate Recombination in Polymer–Polymer Photovoltaic Devices. *J. Chem. Phys.* **2008**, *129*, 114903–114907.
57. Snaith, H. J.; Greenham, N. C.; Friend, R. H. The Origin of Collected Charge and Open-Circuit Voltage in Blended Polyfluorene Photovoltaic Devices. *Adv. Mater.* **2004**, *16*, 1640–1645.
58. Kronik, L.; Shapira, Y. Surface Photovoltage Phenomena: Theory, Experiment, and Applications. *Surf. Sci. Rep.* **1999**, *37*, 1–206.
59. Kronik, L.; Shapira, Y. Surface Photovoltage Spectroscopy of Semiconductor Structures: At the Crossroads of Physics, Chemistry and Electrical Engineering. *Surf. Interface Anal.* **2001**, *31*, 954–965.
60. Dahlberg, S. C.; Musser, M. E. The Surface Photovoltage of an Increasing Series of Polyarenes: Anthracene, Tetracene, and Pentacene. *J. Chem. Phys.* **1979**, *71*, 2806–2810.
61. Musser, M. E.; Dahlberg, S. C. The Surface Photovoltage of Polymethine Semiconducting Films. *J. Chem. Phys.* **1980**, *72*, 4084–4088.
62. Carbone, A.; Pennetta, C.; Reggiani, L. Trapping–Detrapping Fluctuations in Organic Space-Charge Layers. *Appl. Phys. Lett.* **2009**, *95*, 233303.
63. Carbone, A.; Kotowska, B.; Kotowski, D. $f^{\gamma}$ Current Fluctuations in Organic Semiconductors: Evidence for Percolation. *Eur. Phys. J. B* **2006**, *50*, 77–81.
64. Krauss, T.; Brus, L. Charge, Polarizability, and Photoionization of Single Semiconductor Nanocrystals. *Phys. Rev. Lett.* **1999**, *83*, 4840–4843.
65. Cockins, L.; Miyahara, Y.; Grütter, P. Spatially Resolved Low-Frequency Noise Measured by Atomic Force Microscopy. *Phys. Rev. B* **2009**, *79*, 121309.
66. Russell, E. V.; Israeloff, N. E. Direct Observation of Molecular Cooperativity near the Glass Transition. *Nature* **2000**, *408*, 695–698.
67. Coffey, D.; Ginger, D. Patterning Phase Separation in Polymer Films with Dip-Pen Nanolithography. *J. Am. Chem. Soc.* **2005**, *127*, 4564–4565.
68. Segalman, R. A.; McCulloch, B.; Kirmayer, S.; Urban, J. J. Block Copolymers for Organic Optoelectronics. *Macromolecules* **2009**, *42*, 9205–9216.
69. Spitler, E. L.; Dichtel, W. R. Lewis Acid-Catalysed Formation of Two-Dimensional Phthalocyanine Covalent Organic Frameworks. *Nat. Chem.* **2010**, *2*, 672–677.